AGU PUBLICATIONS

JGR

Journal of Geophysical Research: Oceans

RESEARCH ARTICLE

10.1002/2017JC013282

**Key Points:**
- New insights into changes in Ekman dynamics in the western Arctic Ocean when the geostrophic currents become stronger in recent years
- A new mechanism is proposed to explain the stabilization of Beaufort Gyre in recent years
- Several upwelling regions are revealed which may play a significant role in physical and biological processes

**Supporting Information:**
- Supporting Information S1

**Correspondence to:**
W. Zhong,
wlzhong@uw.edu

**Citation:**
Zhong, W., Steele, M., Zhang, J., & Zhao, J. (2018). Greater role of geostrophic currents in Ekman dynamics in the western Arctic Ocean as a mechanism for Beaufort Gyre Stabilization. *Journal of Geophysical Research: Oceans*, *123*. https://doi.org/10.1002/2017JC013282

Received 18 JUL 2017
Accepted 14 DEC 2017
Accepted article online 27 DEC 2017



# Greater Role of Geostrophic Currents in Ekman Dynamics in the Western Arctic Ocean as a Mechanism for Beaufort Gyre Stabilization

**Wenli Zhong[1,2], Michael Steele[2], Jinlun Zhang[2], and Jinping Zhao[1]**

[1]Key Laboratory of Physical Oceanography, Ocean University of China, Qingdao, Shandong, China, [2]Applied Physics Laboratory, University of Washington, Seattle, Washington, USA

**Abstract** Seven different methods, with and without including geostrophic currents, were used to explore Ekman dynamics in the western Arctic Ocean for the period 1992–2014. Results show that surface geostrophic currents have been increasing and are much stronger than Ekman layer velocities in recent years (2003–2014) when the oceanic Beaufort Gyre (BG) is spinning up in the region. The new methods that include geostrophic currents result in more realistic Ekman pumping velocities than a previous iterative method that does not consider geostrophic currents and therefore overestimates Ekman pumping velocities by up to 52% in the central area of the BG over the period 2003–2014. When the BG is spinning up as seen in recent years, geostrophic currents become stronger, which tend to modify the ice-ocean stress and moderate the wind-driven Ekman convergence in the Canada Basin. This is a mechanism we have identified to play an important and growing role in stabilizing the Ekman convergence and therefore the BG in recent years. This mechanism may be used to explain three scenarios that describe the interplay of changes in wind forcing, sea ice motion, and geostrophic currents that control the variability of the Ekman dynamics in the central BG during 1992–2014. Results also reveal several upwelling regions in the southern and northern Canada Basin and the Chukchi Abyssal Plain which may play a significant role in physical and biological processes in these regions.

**Plain Language Summary** New spatial and temporal Ekman dynamics (i.e., horizontal Ekman transport and vertical Ekman pumping) is revealed in the western Arctic Ocean. It was known that the Ekman dynamics is very different under the sea ice. By considering the recent changes of the basin scaled geostrophic current, this study shown that the Ekman dynamics is regulated by the increasing geostrophic current under the sea ice.

## 1. Introduction

The Arctic Ocean is dominated by two large-scale ice and ocean circulations, i.e., the Beaufort Gyre (BG) and the transpolar drift. Spatial variations of wind-induced air-ocean stress (stress at the air-ocean interface) and ice-ocean stress (stress at the ice-ocean interface) result in the divergence and convergence of Ekman transport in surface waters, and thus in upwelling and downwelling, which we broadly refer to here as Ekman pumping. Geostrophic currents also play a role in Ekman pumping by modifying ice-ocean stress (e.g., Hibler, 1979; McPhee, 1975, 1980). The western Arctic Ocean is regulated by the anticyclonic BG circulation which is associated with significant Ekman pumping (e.g., Proshutinsky et al., 2002, 2015). Seeking an Ekman pumping spatial pattern and temporal variability is crucial to understand many processes in this region, including freshwater variability, biological processes, and vertical heat storage or release. In order to evaluate the basin scale Ekman dynamics (i.e., horizontal Ekman transport and vertical Ekman pumping), previous studies have explored several ways to solve this problem. One approach simply involves tracking the changes in hydrographic properties, such as the deepening of the Near-Surface Temperature Maximum layer (NSTM) (e.g., Jackson et al., 2010; McPhee et al., 2009). Hydrographic observations using this approach have shown a clear upwelling region around the Beaufort Sea continental shelf (e.g., Pickart et al., 2009, 2011), while a downwelling region has been observed using the same method in the interior of the Beaufort Gyre (e.g., McLaughlin & Carmack, 2010; Proshutinsky et al., 2009, 2015).

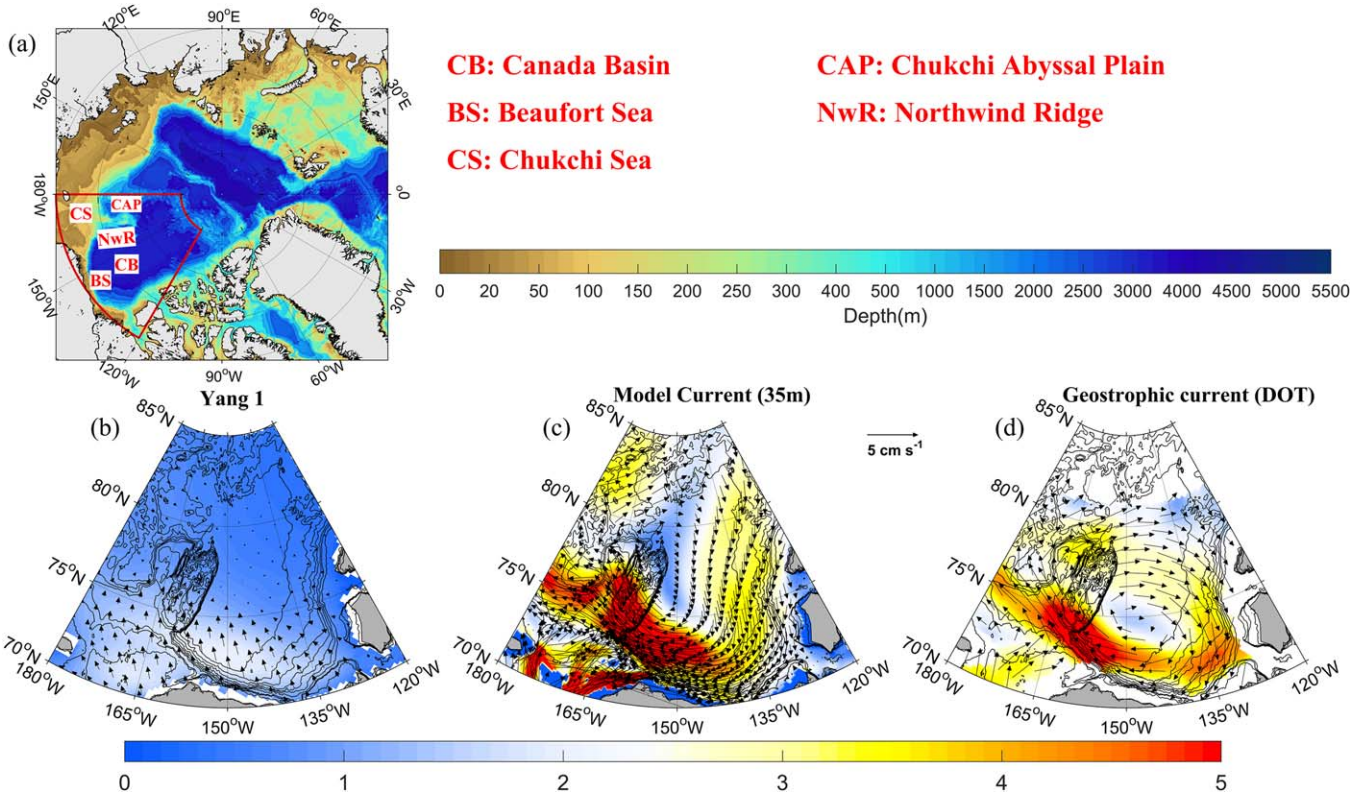


**Figure 1.** (a) The bathymetry of the Arctic Ocean from IBCAO-v3 data (Jakobsson et al., 2012). The western Arctic Ocean where encircled by red line is the study region, bounded by 70–85°N, 120–180°W. Mean ocean surface currents over 2003–2014 derived from three different methods: (b) Ekman layer velocity (iteration method from Yang 1), (c) ocean current (model) at 35 m, assumed to be largely geostrophic (used for Model 3), (d) surface geostrophic current derived from satellite DOT (used for OBSm). The magnitude of the velocity is shown as shading color (unit: cm $s^{-1}$).

A second approach is to combine satellite and reanalysis data to derive the surface stress forcing, wherein the Ekman transport is derived using an iterative method (Ma et al., 2017; Timmermans et al., 2014; Yang, 2006, 2009; Zhong et al., 2015). Using this approach, the mean of upwelling (downwelling) is estimated to be 3.7 $\pm$ 2.0 (–4.0 $\pm$ 2.2) Sv for the entire Arctic Basin during 1979–2014 with a net downwelling of $\sim$0.3 Sv contributed mostly by the Canadian region (Ma et al., 2017). Surface stress at the ocean surface has been changing in recent years (e.g., Martin et al., 2014; Tsamados et al., 2014) and this would result in a different Ekman dynamics. However, this approach generally neglects the effects of geostrophic currents which have been shown to be accelerating in recent years (Armitage et al., 2017; McPhee, 2013; Zhang et al., 2016), as the BG "spins up" in response to changing winds and/or sea ice properties. Many studies have attributed the observed increase in BG freshwater content in recent years to stronger Ekman pumping (e.g., Proshutinsky et al., 2009; Yang, 2009). This increase may saturate when the Ekman transport (induced by the intensification of surface stress) and mesoscale eddy transport reach a balance (Manucharyan & Spall, 2016; Yang et al., 2016). A third approach is to use numerical sea ice-ocean models to directly simulate Ekman dynamics (e.g., Watanabe, 2013; Watanabe & Ogi, 2013; Zhang et al., 2016).

Some previous studies have revealed the important role of ocean currents on Ekman dynamics, especially in a jet stream or eddy (Gaube et al., 2015; Niiler, 1969; Stern, 1965; Wenegrat & Thomas, 2017). In this study, we focus on the effects of geostrophic currents in Ekman dynamics in the western Arctic Ocean (Figure 1a). There are various methods with which to calculate Ekman dynamics in a partially ice-covered ocean. For the sake of completeness, we here use seven different methods to demonstrate, from different aspects, the important and growing role of geostrophic currents in Ekman dynamics in the western Arctic Ocean in recent years. The next section describes the data set and methods used. Section 3 is the comparison of Ekman layer velocity with geostrophic currents which emphasizes the important role of geostrophic currents in Ekman dynamics. In section 4, the new Ekman dynamics and the related processes are revealed. Our major findings and discussions are presented in section 5.

## 2. Data and Methods

### 2.1. Data

Data used in this study include satellite observations, reanalysis data, and model output. Model output is from the Marginal Ice Zone Modeling and Assimilation System (MIZMAS). MIZMAS is a coupled ice-ocean model that assimilates satellite observations of sea ice concentration and SST. Detailed information about MIZMAS model components, domain, and grid configuration can be found in Zhang et al. (2016), where extensive validation against in situ observations from the western Arctic Ocean was also presented. Model sea ice concentration, sea ice motion vectors, sea surface height (SSH), and three-dimensional ocean currents were used for analysis. Model output has an average horizontal resolution in the Chukchi and Beaufort Seas of ~10 km. There are 10 model vertical levels in the upper 50 m of the water column.

Satellite sea ice concentration data were obtained from the Scanning Multichannel Microwave Radiometer (SMMR) on the Nimbus-7 satellite and from the Special Sensor Microwave/Imager (SSM/I) sensors on the Defense Meteorological Satellite Program's (DMSP)-F8, -F11, and -F13 satellites with a resolution of 25 km × 25 km (Comiso, 2000). The retrieval accuracy of this data set is estimated to be ~5–10% in winter and 10–20% in summer at the ice edge. Daily-mean sea level pressure and surface wind over the Arctic Ocean are from the National Center for Environmental Prediction/National Center for Atmospheric Research (NCEP/NCAR) reanalysis with a resolution of 2.5° × 2.5° (Kalnay et al., 1996). The estimated bias of surface wind from this reanalysis is ~0.5 m $s^{-1}$ (~1 m $s^{-1}$) lower than observation in winter (summer) (Lindsay et al., 2014). Daily sea ice motion data are from the Polar Pathfinder daily 25 km EASE-Grid Sea Ice Motion Vectors (Tschudi et al., 2016), with estimated error generally ≤0.8 cm $s^{-1}$ depending on the drift speed, ice concentration, and season (Sumata et al., 2015). The buoy data incorporated in this data set could induce some biases in ice velocity and gradients in daily and weekly averaged field (Szanyi et al., 2016), but this should not affect our analysis, which uses monthly and annual averages.

We also use monthly mean Arctic Dynamic Ocean Topography (DOT) data (2° longitude × 0.5° latitude) from Envisat (2003–2011) and CryoSat-2 (2012–2014) produced by Armitage et al. (2016), with monthly (annual) mean uncertainty of 1.1 (0.9) cm. The grid cells are masked if they are within 10 km of land to avoid contamination. These DOT fields are then used to derive monthly mean geostrophic currents. The Polar Hydrographic Climatology ocean data (1° × 1°) (PHC 3.0) (Steele et al., 2001) are also used to derive the geostrophic current.

All variables from the satellite and reanalysis data are interpolated onto the EASE grid which is used for the Polar Pathfinder sea ice motion (Tschudi et al., 2016) with a resolution of 25 km × 25 km.

### 2.2. Methods

Ocean surface stress in open water areas is a function of the surface wind speed $u_s$. On the other hand, ocean surface stress under sea ice is a function of the difference between ice motion $u_{ice}$ and geostrophic currents $u_{ocean}$ below the Ekman layer. The air-ocean and ice-ocean stresses are expressed using quadratic boundary layer drag laws, i.e., $\vec{\tau}_{air-ocean}=\rho_{air}C_d|\vec{u}_s|\vec{u}_s$ and $\vec{\tau}_{ice-ocean}=\rho_{ocean}C_{iw}|(\vec{u}_{ice}-\vec{u}_{ocean})|R_o(\vec{u}_{ice}-\vec{u}_{ocean})$ (e.g., Hibler, 1979; Hibler & Bryan, 1987; McPhee, 1980), where air density $\rho_{air}=1.25$ kg $m^{-3}$, the air-ocean drag coefficient $C_d=0.00125$, $\rho_{ocean}=1023$ kg $m^{-3}$ is the ocean density, the ice-ocean drag coefficient $C_{iw}=0.0055$ and $R_o$ is rotation matrices for ocean (McPhee, 1975, 1980). A turning angle $\theta=25°$ is used if $\vec{u}_{ocean}$ is the geostrophic current below the boundary layer, as the turning angle usually lies in the range $20° < \theta < 30°$ (McPhee, 1975). The effect of varying drag coefficients on Ekman pumping is discussed in Ma et al. (2017). And the seasonal variability of the ice-ocean drag coefficient could be as large as its variability with different reference ocean current in depth (Cole et al., 2017). For the present work, the widely used value of $C_{iw}=0.0055$ is used so that we can compare with previous studies.

Arctic Ocean surface currents are unfortunately quite poorly observed. Yang (2006, 2009) address this problem by excluding geostrophic currents and assuming that $u_{ocean} = u_{Ekman}$, where $u_{Ekman}$ is the Ekman layer velocity averaged in the Ekman layer, which is solved using a numerical iteration method. This method assumes a constant Ekman layer depth ($D_E = 20$ m), which might be a source of bias. However, using different values of $D_E$ yielded similar results since the Ekman layer velocity is usually considerably smaller than the ice velocity.

**Table 1**
*Summary of Seven Different Methods to Derive Ekman Dynamics*

| Methods[a] | Data | Note |
|---|---|---|
| Yang 1 | Sea ice motion vectors (NSIDC), sea ice concentration (NSIDC), sea level pressure (NCEP/NCAR) | Iterative method to derive Ekman pumping, neglect the geostrophic current (method details in Yang (2006, 2009)) |
| Yang 2 | Sea ice motion vectors (NSIDC), sea ice concentration (NSIDC), 10 m surface wind (NCEP/NCAR) | Same to Yang 1 to derive Ekman pumping |
| Yang 3 | Sea ice motion vectors (MIZMAS model), sea ice concentration (MIZMAS model), 10 m surface wind (NCEP/NCAR) | Same to Yang 1 to derive Ekman pumping |
| Model 1 | Ocean surface stress (MIZMAS model): $\vec{\tau}_{ocn}=\vec{\tau}_{air}+\vec{F}_i$($\vec{F}_i$is the ice interaction force), where $\vec{\tau}_{air}=(1-\alpha)\vec{\tau}_{air-ocean}+\alpha\vec{\tau}_{air-ice}$(details see Martin et al., 2014) | Ekman pumping: $w=\nabla\times\vec{\tau}_{ocn}/(f\rho)$ |
| Model 2 | Vertical velocity at 30 m depth (MIZMAS model) | Vertical velocity: $w=\int_{-h}^{\eta}[-(\nabla\cdot\vec{V}_h)]dz$ |
| Model 3 | Sea ice motion vectors (MIZMAS model), sea ice concentration (MIZMAS model), 10 m surface wind (NCEP/NCAR), ocean current at 35 m depth (MIZMAS model) | As in Yang 3, but ice-ocean stress calculated using model ocean current: $w=\nabla\times\vec{\tau}_{total}/(f\rho)$ |
| OBSm | Sea ice motion vectors (NSIDC), sea ice concentration (NSIDC), sea level pressure (NCEP/NCAR), surface geostrophic current derived from DOT Armitage et al. (2016) | Similar to Model 3, but using DOT observed ocean currents: $w=\nabla\times\vec{\tau}_{total}/(f\rho)$ |

[a]Yang 1, Yang 2, and Yang 3 (no geostrophic current is used), Model 1, Model 2, and Model 3 (geostrophic current implied by the model is used), OBSm (geostrophic current from observation is used).

In this work, we extend Yang's method to derive Ekman pumping using three methods (Table 1). Our first method (denoted as "Yang 1") is exactly that described by Yang, which uses sea level pressure data to derive surface winds, sea ice concentration from satellite observations, and sea ice motion vectors from satellite and buoy observations. The second method (denoted as "Yang 2") is the same as Yang 1, but it uses surface winds (at 10 m) from the reanalysis product directly. The third method (denoted as "Yang 3") also employs the same strategy as Yang 1, but uses as input reanalysis surface winds, model sea ice concentration, and model sea ice motion vectors. This method is introduced so that we can compare the difference of Ekman dynamics among different model-based methods that either incorporate the geostrophic currents or do not (see below). Ekman pumping velocity is then calculated as: $w=\nabla\times\vec{\tau}_{total}/(f\rho)$ (where $\vec{\tau}_{total}=(1-\alpha)\vec{\tau}_{air-ocean}+\alpha\vec{\tau}_{ice-ocean}$, $\alpha$ is the ice concentration).

The next approaches described here rely heavily on model output. The first model method (denoted as "Model 1") uses MIZMAS modeled total ocean surface stress $\vec{\tau}_{total}$ to calculate Ekman pumping, where the model calculates ice-ocean stress $\vec{\tau}_{ice-ocean}$ using the "embedded ice" method (e.g., Martin et al., 2014), which depends only on air-ice and ice internal stresses. "Model 1" is from the MIZMAS model run in which ice-ocean stress (used to calculate sea ice motion, deformation, and internal interaction force) is calculated using the ocean velocity at the seventh level (centered at 32.5 m depth) to approximate geostrophic surface currents. This follows the method of Hibler and Bryan (1987), based on the boundary layer theory of McPhee (1975). The second model method (denoted as "Model 2") simply uses modeled vertical velocity (as computed by the divergence of horizontal currents) at 30 m depth, to compare with Ekman pumping velocities. The third model method (denoted as "Model 3") is similar to Yang 3, but instead of using iteratively derived Ekman layer velocities to approximate $u_{ocean}$, it uses the ocean current taken at model level 7 (at 35 m depth), which is likely below the boundary layer or the mixed layer (Peralta-Ferriz & Woodgate, 2015) and thus the current at that level is assumed to be the geostrophic current.

Our final method is similar to Model 3, except that it uses the satellite-derived DOT monthly mean surface geostrophic currents to calculate ice-ocean stress, in combination with satellite observed sea ice concentration, sea ice motion vectors, and surface winds. This method does not use any ice-ocean model output, nor does it use Yang's iterative method to calculate ocean surface currents. We thus denote the results from this observation-based method as "OBSm." The time period of the DOT data is 2003–2014; in order to extend the time series of this method, the monthly climatology PHC-derived geostrophic current is also used for the period of 1992–2002 (used repeatedly for each year). For all the methods with daily inputs, Ekman pumping was calculated based on daily data and then averaged to obtain the monthly mean fields used here for analysis. Further details of these seven methods are listed in Table 1.

We also considered an extension of the OBSm that accounts for the relative vorticity of ocean currents in regions of strong shear (e.g., on the southwestern flank of the BG). Many studies have explored this effect (Gaube et al., 2015; Niiler, 1969; Wenegrat & Thomas, 2017) and have found that when the Rossby number of the ocean current approaches unity, the relative vorticity $\zeta$ should be considered when calculating Ekman pumping, i.e., using $W_E = \nabla \times \left[\vec{\tau}/(f+\zeta)\right]/\rho_0$ (Stern, 1965). We used this formula to modify our OBSm, but found negligible difference because the Rossby number is still much smaller than unity everywhere in our domain. This method was thus not included in the analysis below.

## 3. Comparison of Ekman Layer Velocity With Geostrophic Current

First, we compare the magnitude of the Ekman layer velocity (derived using method Yang 1) with the surface geostrophic current over the years 2003–2014. Figure 1b shows that the Ekman layer velocity is very different in direction (as expected) and in many places much smaller in magnitude relative to the geostrophic current. The largest derived Ekman layer velocity is $<$2.5 cm $s^{-1}$, while the geostrophic current exceeds 5 cm $s^{-1}$. The maximum of Ekman layer velocity appears in the southern Beaufort Sea where easterly winds prevail. Although there is a difference between the model and DOT results regarding the position of BG center, they both show the strongest geostrophic currents at the periphery of the BG, with the maximum velocity at the southern and southwestern Canada Basin and relatively weaker velocity on the northern limb of the BG. Two reasons may contribute to this north-south asymmetry: (1) the sea ice motion is more mobile at the southern Canada Basin and (2) the freshwater dome has its largest gradient in the south, which results in a stronger geostrophic current. The model methods (Model 1 and Model 3) have smaller Ekman layer velocity at the southern limb of BG compared with Yang 1, Yang 2, and Yang 3 (figures not shown). We will discuss this further below. In the northern Chukchi Sea, the model velocity field (Figure 1c) captures the well-known three branches of canyon-steered northward-flowing water (Weingartner et al., 2005) while the lower-resolution DOT-derived geostrophic current (Figure 1d) does not show a hint of these three branches. The lack of these fine-scale currents in the DOT-derived fields might be related to the Gaussian smoothing function applied to the DOT data that has a standard deviation of 100 km (Armitage et al., 2016).

## 4. The Effects of Geostrophic Current on Ekman Dynamics

### 4.1. New Spatial Patterns and Temporal Variability of Ekman Dynamics

Figure 2 shows the multiyear mean Ekman pumping velocity using the seven different methods. A significant difference is that Ekman pumping in the center of the BG (the maximum downwelling area in the Canada Basin) is much smaller when considering the geostrophic current. Further, the position of the BG center is not the same among different methods; the reasons for this will be discussed in section 4.3. In the Chukchi Sea and Chukchi Borderland, Figure 2 shows that the OBSm and Model 1, Model 2, and Model 3 all predict a relatively strong downwelling of 6–10 cm $d^{-1}$ or higher, a value larger than that found in the center of the BG. An interesting phenomenon is that the spatial pattern of downwelling in the Chukchi Sea shows some possible bathymetric influence, i.e., at the Chukchi shelf break and along the east of Chukchi Abyssal Plain. This downwelling region was also discussed with respect to Pacific Water mass subduction by Timmermans et al. (2014). On the other hand, the OBSm shows no obvious bathymetric influence, likely a result of the coarse spatial and temporal resolution of the geostrophic current data. Another interesting difference apparent in Figure 2 is the appearance of patchy areas of upwelling in the southern and northern Canada Basin and the Chukchi Abyssal Plain in the OBSm and Model 1, Model 2, and Model 3 results, in contrast to the general downwelling found in these areas using Yang 1, Yang 2, and Yang 3. The location of these upwelling patches is at the periphery of BG, where geostrophic currents are strong and thus Yang's method becomes questionable (Timmermans et al., 2014; Yang, 2009).

All seven methods show a high correlation with each other in monthly variability (Figures 3a, 3b, and Table 2), especially those that use the same wind forcing and sea ice motion forcing (i.e., Yang 1, Yang 2, and OBSm). In the central Canada Basin (the area encircled by thick black line in Figure 2), the 2003–2014 mean Ekman pumping velocities using OBSm, Model 1, Model 2, and Model 3 are 50%, 45%, 52%, and 40% weaker than those computed using Yang 1, respectively. Further, the methods that neglect the effect of

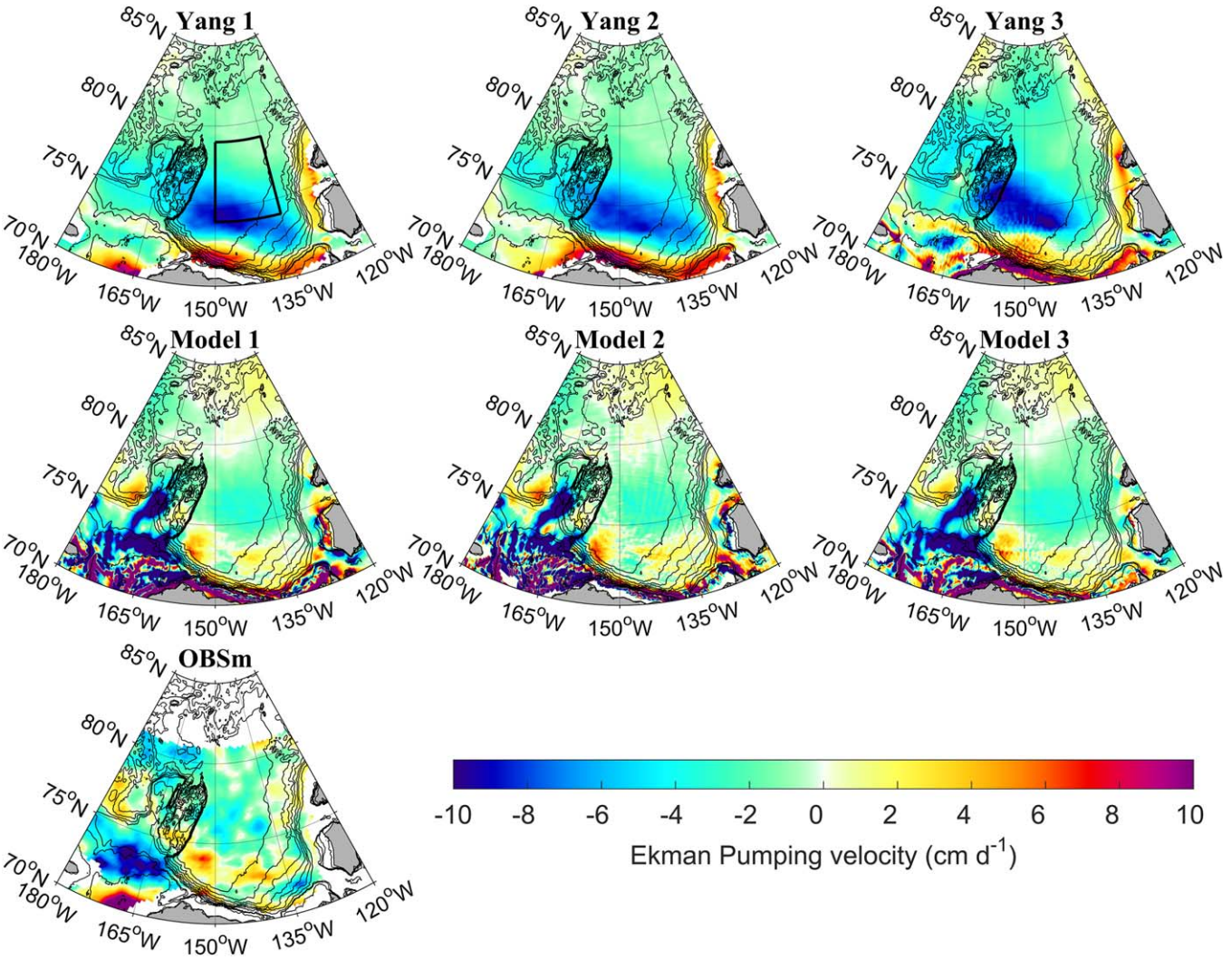


**Figure 2.** Mean Ekman pumping velocity over 1992–2014 using different methods (unit: cm $d^{-1}$), except for Model 2, which is the total model vertical velocity at 30 m, and "OBSm" which provides the mean over 2003–2014. The area (74–79°N, 135–150°W) encircled by thick black line is referred to as the central Canada Basin following Timmermans et al. (2014).

geostrophic currents have a different position of the multiyear mean BG center compared with those that take this effect into account. The time series comparison in Figure 3 is from the spatial mean in the domain of 74–79°N, 135–150°W which is referred to as the central Canada Basin. This domain is coherent with the multiyear mean BG center using model methods and OBSm while the Yang's methods show a more southern BG center around 74.5°N, 150°W. Another time series comparison is made for the spatial mean within a 150 km radius of the multiyear mean BG center from different methods (supporting information Figures S1 and S2). Similar results are shown in supporting information Figure S2 but with a much larger Ekman downwelling using Yang's methods especially during 2000–2014 (supporting information Figure S2c). All the methods show relatively large downwelling in 1998 and in 2007, while all the model methods also show relatively large downwelling in 1995 and 1997. The amplitude of downwelling is reduced using the three model methods and OBSm, relative to the three Yang's methods (Figures 3c, 3d and supporting information Figures S2c, S2d). The OBSm has a higher correlation coefficient with all model methods than with the Yang's methods in annual mean during 2003–2014. All Yang's methods show an increase of downwelling during 2007–2014 compared with 1999–2006, while there is no such difference using Model 1, Model 2, Model 3, and OBSm (Figures 3c, 3d and supporting information Figures S2c, S2d). The reasons for this will be discussed later.

All methods show a clear seasonal variability of Ekman pumping, with generally larger seasonal amplitude since 2003 (Figure 4). For example, the Ekman pumping in fall (October to December) is generally $<5$ cm $d^{-1}$

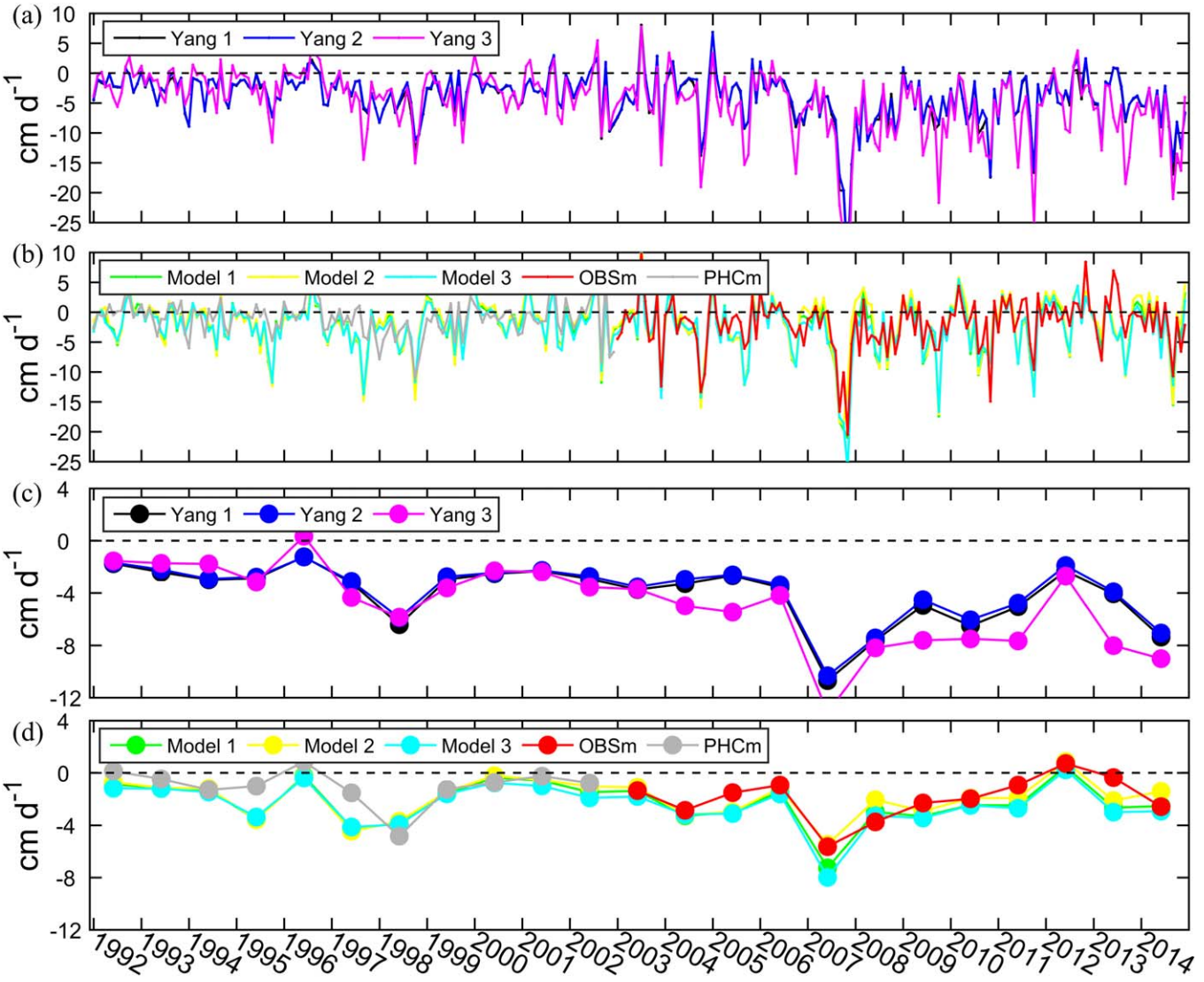


**Figure 3.** Ekman pumping velocity of different methods within 74–79°N, 135–150°W (the area encircled by thick black line in the first plot of Figure 2) during 1992–2014. The PHC-derived geostrophic current is used for the calculation of ice-ocean stress (and thus the final Ekman pumping velocity) during 1992–2002 which denoted as "PHCm." (a and b) Monthly variability and (c and d) annual variability. The annual mean correlation coefficients between OBSm and Yang 1 (Yang 2, Yang 3, Model 1, Model 2, Model 3) is 0.84 (0.84, 0.75, 0.86, 0.79, 0.86), respectively, during 2003–2014 in Figures 3c and 3d. Notice the different vertical scales in Figures 3c and 3d comparing with the Figures 3a and 3b.

in 1992–2002 from all methods (except OBSm which does not have annual mean geostrophic current during 1992–2002), while it is ~10 cm $d^{-1}$ from September to December in 2003–2008 with all Yang's methods. The Ekman pumping from all the model methods and OBSm is approaching 10 cm $d^{-1}$ on September and October but reduced considerably by November and December during 2003–2008. The Ekman pumping is smaller from September to December in 2009–2014 from all methods (Figure 4). Details of the controlling mechanisms as well as our rationale for choosing these time periods will be discussed in section 4.4.

### 4.2. Validation of Model Geostrophic Current

Is the model estimate of geostrophic current reasonable, relative to observations? In order to answer this question, we compare in Figure 5 the modeled SSH and corresponding geostrophic currents with similar fields computed using the PHC climatology and the satellite DOT. Figures 5a–5c show that the center of the BG was near the Northwind Ridge before 2003. Satellite observations indicate that this center shifted to the southeastern Canada Basin during 2003–2008, and back toward the Northwind Ridge during 2009–2014, similar to the findings of Armitage et al. (2017). Although the model SSH fails to reproduce the shifting

**Table 2**
*Correlation Coefficient Between Ekman Pumping Velocity Using Different Methods (Correlation of Monthly Variability, the Time Series Variabilities are Shown in Figures 3a and 3b)*

| Yang 1 | Yang 2 | Yang 3 | Model 1 | Model 2 | Model 3 | | Ekman pumping (mean)/cm $d^{-1}$ |
|---|---|---|---|---|---|---|---|
| 0.92 | 0.90 | 0.77 | 0.80 | 0.74 | 0.83 | OBSm | (−2.1)[a] |
| | 0.99 | 0.86 | 0.75 | 0.67 | 0.81 | Yang 1 | −4.1 (−4.2) |
| | | 0.86 | 0.73 | 0.64 | 0.80 | Yang 2 | −3.9 (−3.9) |
| | | | 0.88 | 0.81 | 0.92 | Yang 3 | −4.9 (−5.0) |
| | | | | 0.98 | 0.98 | Model 1 | −2.3 (−2.3) |
| | | | | | 0.95 | Model 2 | −1.9 (−2.0) |
| | | | | | | Model 3 | −2.5 (−2.5) |

[a]Not available in 1992–2002.

*Note*. The correlation coefficient between "OBSm" and the other six methods is calculated from the time period of 2003–2014 (first row) while the others are from time period of 1992–2014. The correlation coefficient all pass the significance level of 95% ($p < 0.05$). All of these correlation coefficients are within 10% of each other with or without the seasonal signal removed. The 1992–2014 mean Ekman pumping velocities (cm $d^{-1}$) from different methods are shown as the number in the last column of the table where the numbers in parentheses are the 2003–2014 means.

position of BG during 2003–2014 (Figures 5e and 5f), the model does show a similar increase of geostrophic current in the central Canada Basin (also a similar increase/decrease of southwestern/southeastern geostrophic current). This is illustrated by the high correlation coefficient ($r = 0.65$, $p < 0.05$) between model SSH-derived geostrophic current and DOT-derived geostrophic current in the central Canada Basin (Figure 5g). The model geostrophic current has much larger spatial variance relative to the DOT-derived geostrophic current, likely owing to the model's higher spatial and temporal resolution.

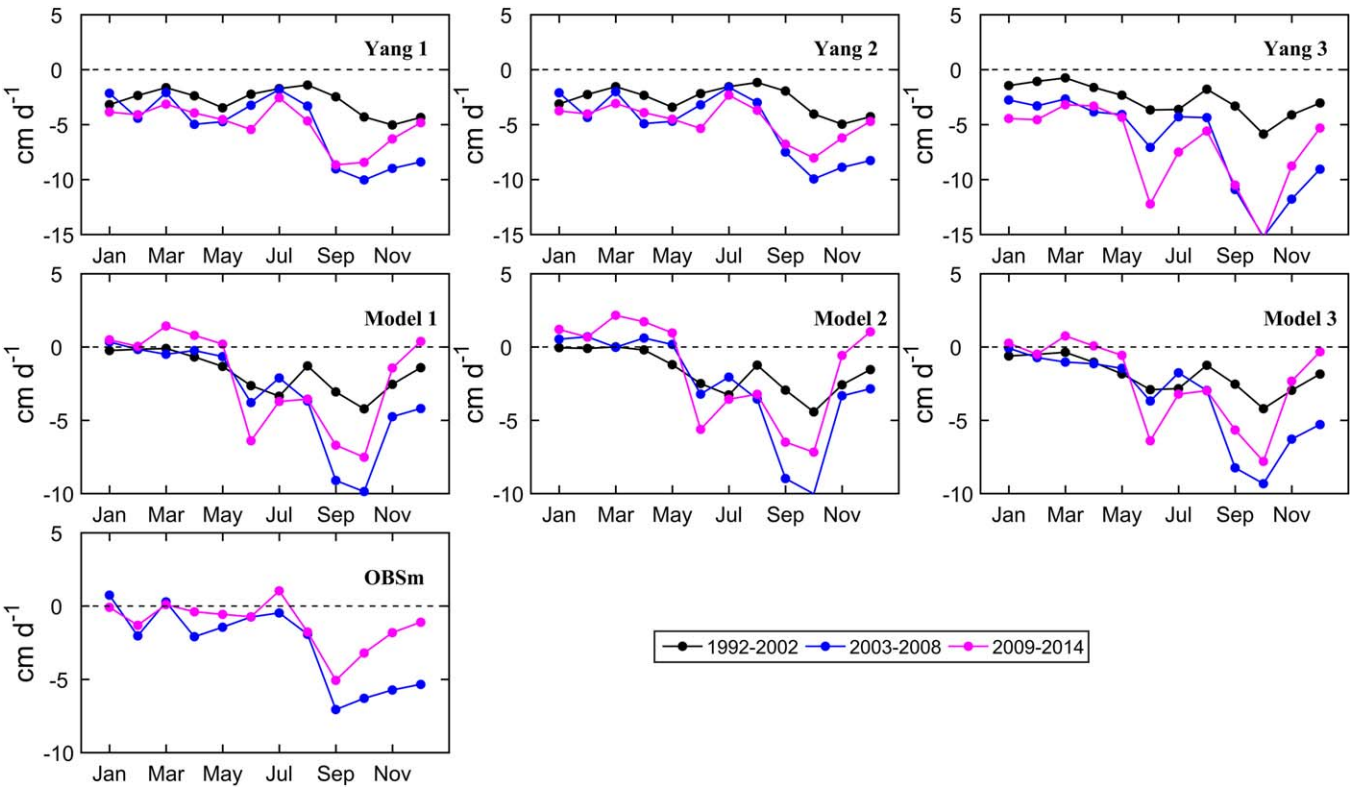


**Figure 4.** Monthly variability of Ekman pumping velocity using different methods within 74–79°N, 135–150°W (the area encircled by thick black line in the first plot of Figure 2) for three periods, i.e., 1992–2002, 2003–2008, 2009–2014. Notice the different vertical scale in Model 1, Model 2, Model 3, and OBSm comparing with Yang 1, Yang 2, and Yang 3.

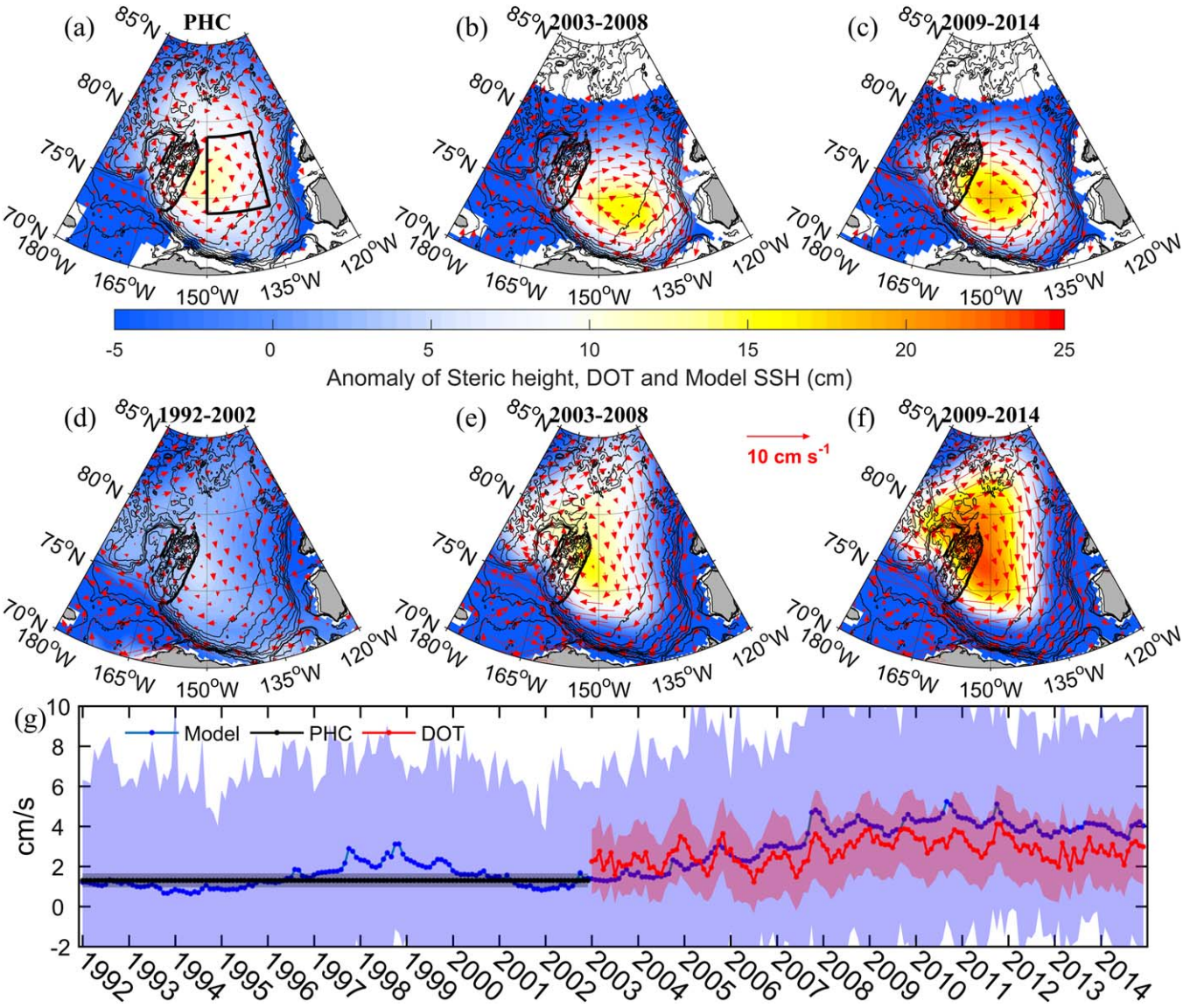


**Figure 5.** (a) Anomaly of PHC-derived steric height (cm) relative to 1,000 dbar or the depth of the ocean bottom, depending on which is shallower, (b and c) anomaly of Dynamic Ocean Topography (DOT, cm) based on the Envisat and CryoSat-2 observation, (d–f) anomaly of Model SSH (cm). "Anomaly" here is defined for each field relative to its mean value over the region 70–81.5°N, 120–180°W. The red vectors are the derived geostrophic current from different fields. (g) The spatial mean magnitude of geostrophic current in the domain of 74–79°N, 135–150°W (the area encircled by thick black line in Figure 5a) derived from model SSH (blue dot line), PHC (black dot line), and DOT (red dot line), shading color indicates plus or minus one standard deviation of geostrophic current in the defined domain. The correlation coefficient between model-derived geostrophic current and DOT-derived geostrophic current during 2003–2014 is 0.65 ($p < 0.05$).

### 4.3. Contribution of Ice-Ocean Stress to Ekman Dynamics

What is the main reason for the differences in Ekman dynamics between Yang 1, Yang 2, and Yang 3 versus Model 1, Model 2, and Model 3 and OBSm? The answer is the effect of geostrophic currents, which have a large impact on ice-ocean stress in the western Arctic Ocean (Figure 6). To illustrate this point, we compare the Yang 3 and Model 3, since the only difference between these two methods is that model geostrophic velocity is used in Model 3 instead of using the iteratively derived Ekman layer velocity in Yang 3. We also compared Yang 1 and OBSm (figures not shown) and found similar results. Both Yang 3 and Model 3 show an intensification in fall (November) and winter (February) with relatively weak amplitude in summer (August). Significant differences in the ice-ocean stress curl between the two methods (Figures 6a and 6b) appear in February, May, and November, i.e., Model 3 shows many divergence patches in the southern and northern Canada Basin and the Chukchi Abyssal Plain while Yang 3 shows an overall convergence. Fewer differences

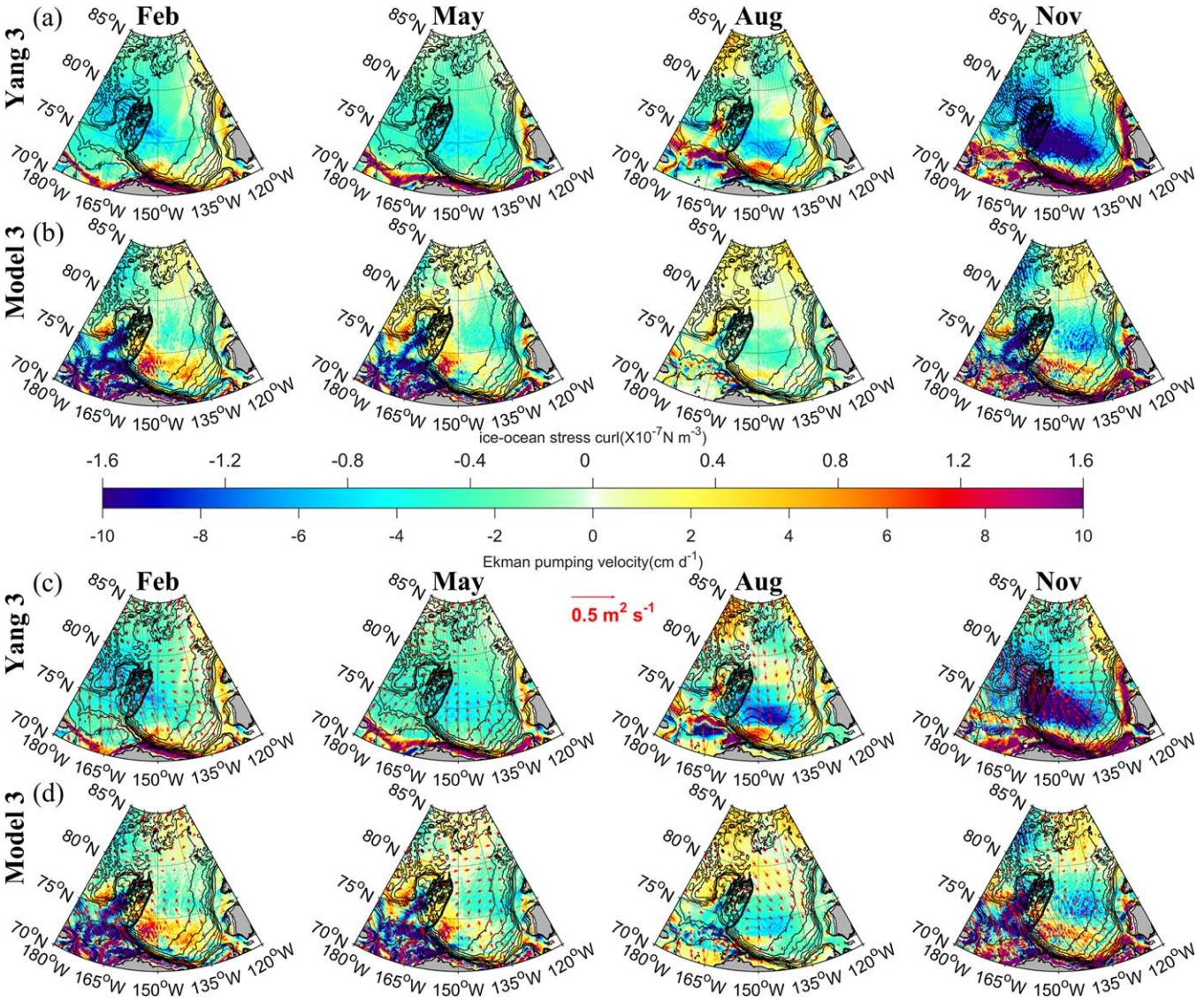


**Figure 6.** Seasonal variability of (a) and (b) ice-ocean stress curl ($\times 10^{-7}$ N m$^{-3}$), (c) and (d) Ekman pumping (cm d$^{-1}$) during 1992–2014 using Yang 3 and Model 3 (color shading). The Ekman transport (m$^2$ s$^{-1}$) are shown as red vectors in Figures 6c and 6d.

are seen in August when the geostrophic current is relatively weak (supporting information Figure S3). The spatial pattern of Ekman pumping (Figures 6c and 6d) is similar to the ice-ocean stress curl (Figures 6a and 6b), which indicates that, even with a shrinking sea ice cover, the ice-ocean stress curl has more influence on the long-term mean Ekman pumping than the air-ocean stress curl. Large areas of upwelling patches appear in the southern Canada Basin in February and November while significant upwelling appears in the Chukchi Abyssal Plain in May, August, and November in Model 3 contrasting to Yang 3 method. This is coherent with the spatial changes of ice-ocean stress curl which indicates the difference comes from seasonal changes of geostrophic currents. In addition, not only has the direction of Ekman transport changed, but also the magnitude is significantly reduced when considering the geostrophic current using Model 3 (Figures 6c and 6d). And this results in a different BG extent which is also shown in Figure 2.

### 4.4. The Long-Term Changes of Ekman Dynamics in the Beaufort Gyre

The changes of Ekman dynamics during 1992–2014 are here divided into three subperiods (Figure 7), with two extraordinary years (2007 and 2012) also noted in Figure 3. During period 1 (1992–2002), the wind forcing, the sea ice motion and geostrophic current are generally weak (not shown). The Yang 3 method

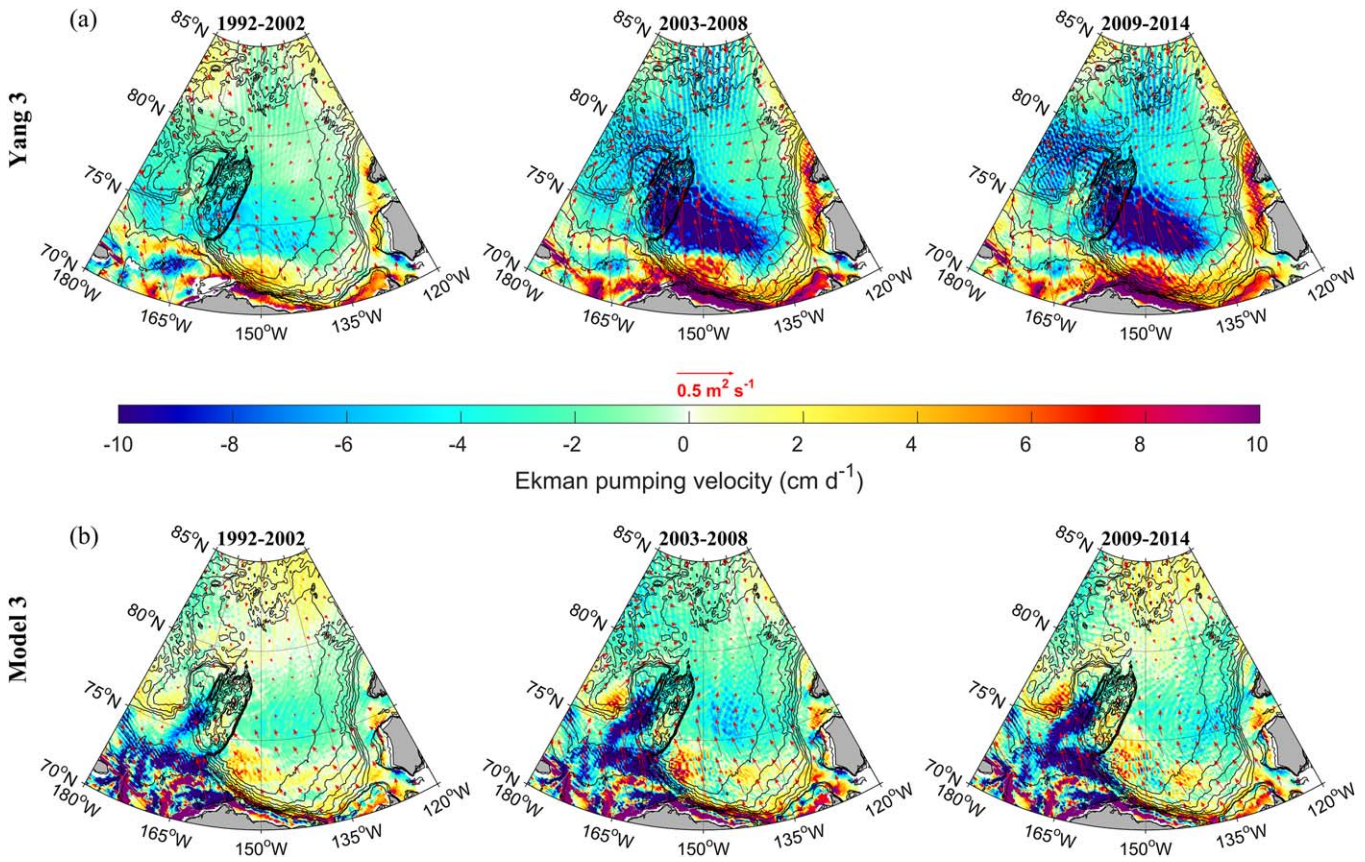


**Figure 7.** Multiyear mean of Ekman pumping (color shading) and Ekman transport (red vectors) in three periods (1992–2002, 2003–2008, 2009–2014) using two methods: (a) Yang 3 and (b) Model 3.

(Figure 7a) shows an overall downwelling in the basin, while Model 3 (Figure 7b) shows relatively weak downwelling and some upwelling in the northern Canada Basin, the northern Beaufort Sea, and the Chukchi Abyssal Plain. Also Model 3 shows relatively strong downwelling along the Chukchi shelf break and in the east of Chukchi Abyssal Plain which are much stronger than that inside the BG. During period 2 (2003–2008), again the Yang 3 shows an overall downwelling that is particularly strong in the southern Canada Basin. On the other hand, Model 3 shows a rather weak downwelling (also intensified) in the central Canada Basin and accompanied by intensified upwelling in the southwestern Canada Basin. The most noticeable phenomenon is that Model 3 shows significant increases of downwelling in the Chukchi Sea which are much stronger than that inside the BG. Both methods show an increase of Ekman transport (red vectors in figure) toward the BG center when compared to period 1. The maximum of Ekman transport occurs mostly in the southwestern Canada Basin using Yang 3 while Model 3 has a relatively larger area of maximum Ekman transport extending toward the central Canada Basin (74–79°N, 135–150°W). During period 3 (2009–2014), there is hardly change of downwelling in the Chukchi Sea using Model 3, while there are some upwelling patches there in Yang 3. The Yang 3 shows that downwelling inside the BG is comparable with period 2, while Model 3 shows a slightly weaker downwelling than period 2. The magnitude of Ekman transport from Model 3 seems to be comparable in both periods 2 and 3. So a question arises: is there a significant change of Ekman dynamics in the BG during 1992–2014? It is obvious that there is an increase of Ekman downwelling inside the BG since the start of this century, as revealed by many other studies (e.g., Proshutinsky et al., 2015; Timmermans et al., 2014). But is there really a noticeable increase of downwelling in the BG during 2008–2014 comparing with 2002–2006 as shown in Figure 3c and supporting information Figure S2c using all the Yang's methods (excluded the year 2012)? In contrast to Yang's methods, all the model methods and OBSm show a general increase in Ekman downwelling during 2002–2007 and then a rather stable variation during 2008–2014 (Figure 3d and supporting information Figure S2d).

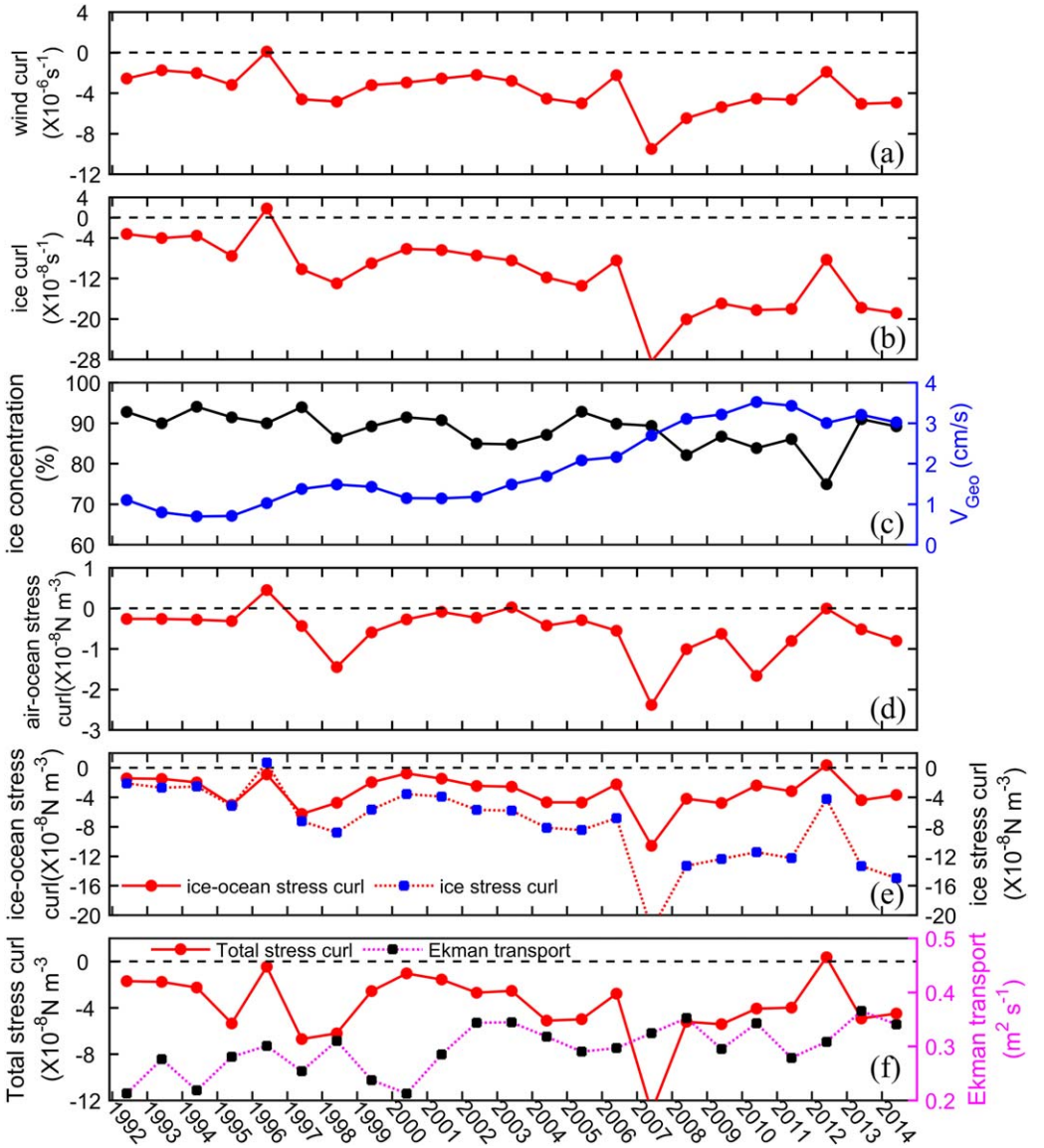


**Figure 8.** (a) Wind curl ($\nabla\times\vec{u}_{wind}$), (b) ice motion curl ($\nabla\times\vec{u}_{ice}$), (c) ice concentration and geostrophic current, (d) air-ocean stress curl ($\nabla\times((1-\alpha)\vec{\tau}_{air-ocean}$)(, (e) ice-ocean stress curl ($\nabla\times(\alpha\vec{\tau}_{ice-ocean})$) and ice stress curl ($\nabla\times(\alpha\vec{\tau}_{ice})$), (f) total stress curl $\left(\nabla\times\left[(1-\alpha)\vec{\tau}_{air-ocean}+\alpha\vec{\tau}_{ice-ocean}\right]\right)$ and Ekman transport (i.e., Ekman layer velocity multiplied by Ekman layer depth: $\vec{U}_E=\vec{u}_E\cdot D_E$) from the MIZMAS model in the domain of 74–79°N, 135–150°W during 1992–2014. In order to evaluate the effects of the geostrophic current, the ice stress curl is calculated by neglecting the geostrophic current in the ice-ocean stress curl such that $\nabla\times(\alpha\vec{\tau}_{ice})=\nabla\times(\alpha\rho_{water}C_{iw}|\vec{u}_{ice}|\vec{u}_{ice})$, where $\alpha$ is the sea ice concentration. Results from Model 3 are used for illustration in Figures 8e and 8f.

In order to answer the above question, we separate some key parameters that may contribute to changes in Ekman dynamics during the whole study period. These parameters are: wind curl, ice motion curl, ice concentration, geostrophic current, air-ocean stress curl, ice-ocean stress curl, ice stress curl (neglecting the geostrophic current in the formulation of ice-ocean stress), total surface stress curl, and Ekman transport (Figure 8). All these parameters are spatially averaged within the domain of 74–79°N, 135–150°W defined as the central Canada Basin, calculated from MIZMAS model (except the wind curl which is derived from the NCEP/NCAR data). The negative wind curl shows an increase during 2007–2014 compared to 1997–2006, while the negative ice motion curl shows much larger increases comparing these two periods (Figures 8a and 8b). The annual mean ice concentration does not show a significant decreasing trend in the central

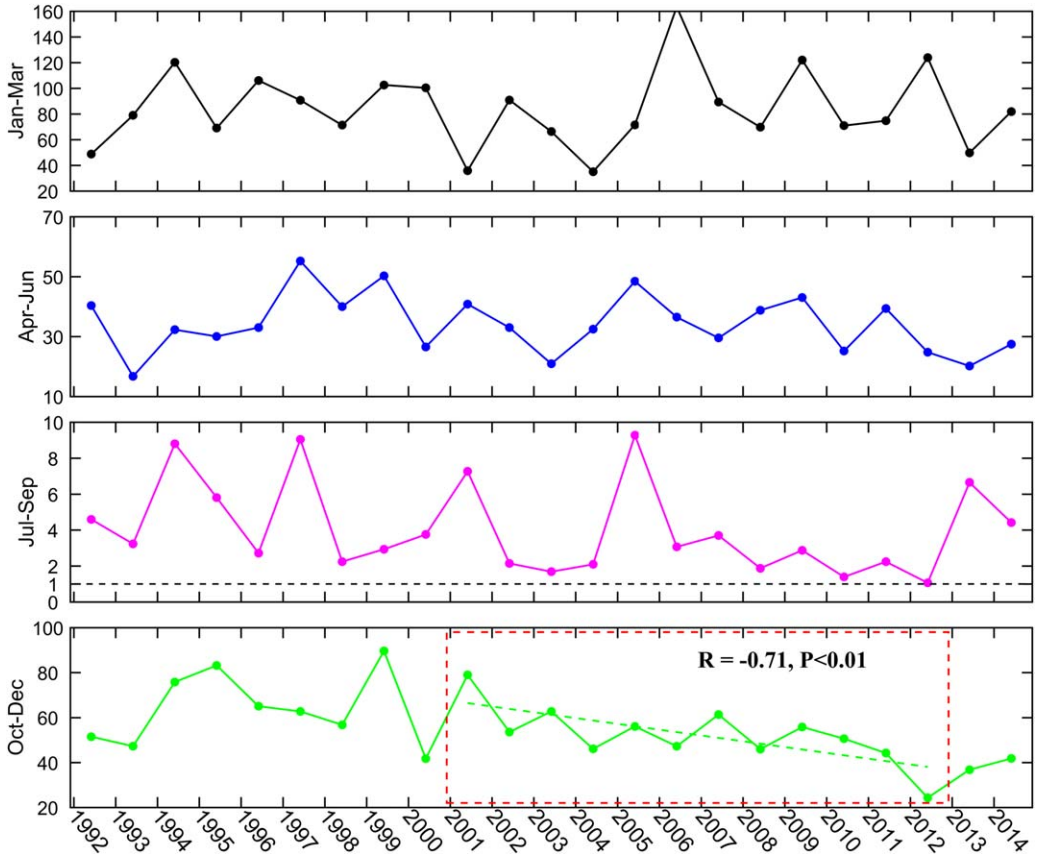


**Figure 9.** The median ratio of relative contributions from the ice-ocean stress curl and that from the air-ocean stress curl (see the text for the definition) during 1992–2014 in different seasons from MIZMAS model in the domain of 74–79°N, 135–150°W (The area encircled by thick black line in the first plot of Figure 2). The red dashed box was chosen as the period (2001–2012) when geostrophic current increased (Figure 8c); here it shows a period of decreasing curl ratio. The linear fit (green dashed line) has a slope of −0.26 with a 95% confidence interval between −0.34 and −0.18.

Canada Basin, with a minimum value in 2012 (Figure 8c, black dot line). The geostrophic current shows a gradually increase since 1996 and reaches a maximum in 2010, it then becomes stabilized if not relaxing slightly (Figure 8c, blue dot line). The total stress curl can be divided into two parts: $\nabla\times\vec{\tau}_{total}=\nabla\times((1-\alpha)\vec{\tau}_{air-ocean})+\nabla\times(\alpha\vec{\tau}_{ice-ocean})$, where the first term is the air-ocean stress curl and the second term the ice-ocean stress curl. The air-ocean stress curl shows three maximum values in 1998, 2007, and 2010 while the ice-ocean stress curl shows three maximum values in 1995, 1997, and 2007 (Figures 8d and 8e). The ice-ocean stress curl has higher magnitude than the air-ocean stress curl, and is the dominant term in the final total stress curl (Figure 8f). This is also reflected in Figure 6 as the ice-ocean stress curl dominates the spatial pattern of final Ekman pumping. To see how the geostrophic current alters the ice-ocean stress curl, the ice stress curl is calculated by neglecting the geostrophic current in the formulation of ice-ocean stress (Figure 8e). One can see that excluding the geostrophic current, the ice stress curl is much larger than the ice-ocean stress curl without the ice-ocean shear. Significantly, there is a general increase of ice stress curl during 2007–2014 when compared to 1997–2006. The nonlinear term of the stress formula has amplified the increases of the ice motion curl (Figure 8b). Before 1998, the geostrophic current is small with a value of ∼1 cm $s^{-1}$ and the amplitude of ice-ocean stress curl and ice stress curl are comparable and their difference is small (Figure 8e). But as the geostrophic current begins to increase from 1998, the curve of ice stress curl begins to deviate from the curve of ice-ocean stress curl, i.e., their difference becomes larger. The difference between ice stress curl and ice-ocean stress curl becomes generally larger in 2007–2014 than in 1998–2006. Note that all the Yang's methods have shown a continued increase of Ekman downwelling during most of 2008–2014, relative to 2002–2007, while all the model methods and OBSm show a rather stable variation during 2002–2014 (Figures 3c, 3d and

supporting information Figures S2c, S2d). The increases of geostrophic current act as a buffer to moderate the increases of Ekman pumping in later periods. Also, the Ekman transport in the central Canada Basin shows a rather stable variation during 2002–2014 (Figure 8f). The Ekman layer velocity could be readily obtained from the Ekman transport by dividing the Ekman layer depth (used as a constant 20 m).

From Figures 6c and 6d, we know that the sea ice cover is important for providing the dominant term of ice-ocean stress curl in the final Ekman pumping. In order to evaluate the contributions from the air-ocean stress curl and ice-ocean stress curl to the long-term changes of Ekman pumping, we define the ratio of relative contribution from the ice-ocean stress curl and that from the air-ocean stress curl as:

$$ratio = \frac{|\nabla\times((1-\alpha)\vec{\tau}_{air-ocean})-\nabla\times\vec{\tau}_{total}|}{|\nabla\times(\alpha\vec{\tau}_{ice-ocean})-\nabla\times\vec{\tau}_{total}|}$$

where $\vec{\tau}_{total}=(1-\alpha)\vec{\tau}_{air-ocean}+\alpha\vec{\tau}_{ice-ocean}$. This is an inverse ratio from the absolute difference of the ice-ocean stress curl and the total stress curl divided by the absolute difference of the air-ocean stress curl and the total stress curl. When the ratio is larger than 1, the ice-ocean stress curl has more influence on the Ekman pumping than the air-ocean stress curl, otherwise it has less influence. Figure 9 shows the seasonal changes of this ratio. Here the median value is used to give a better idea of a "typical" ratio, so that it is not skewed so much by extremely large or small values. The median value is determined by finding the median value of data points within the domain of 74–79°N, 135–150°W. The ratio has the highest value on January–March following by October–December, April–June, and July–September. Almost all the ratio is much larger than unity which again indicates the ice-ocean stress curl is the dominated term in the total stress curl and thus the Ekman pumping. This ratio is almost always less than 10 on July–September throughout the whole study period and almost equal to unity in 2012. The ratio on October–December shows a decreasing trend especially during 2001–2012 when the geostrophic current substantially increases (Figure 8c). This indicates that the contributions from the ice-ocean stress curl to the Ekman pumping is decreasing when the geostrophic current significantly increases, especially on October–December when both the sea ice motion and geostrophic current reach their maximum during the year. The effects of the reducing ratio on the final Ekman pumping are also shown in Figure 4 using all model methods and OBSm as a significantly reduces of Ekman pumping on September–December in 2009–2014 comparing with 2003–2008. The BG gains most of the freshwater in fall (October–December) but the intensification of geostrophic current tend to reduce or deprive its freshwater gaining capacity. The ratio shows a rebound in all seasons as the sea ice concentration (Figure 8c) shows a similar rebound in central Canada Basin in 2013–2014.

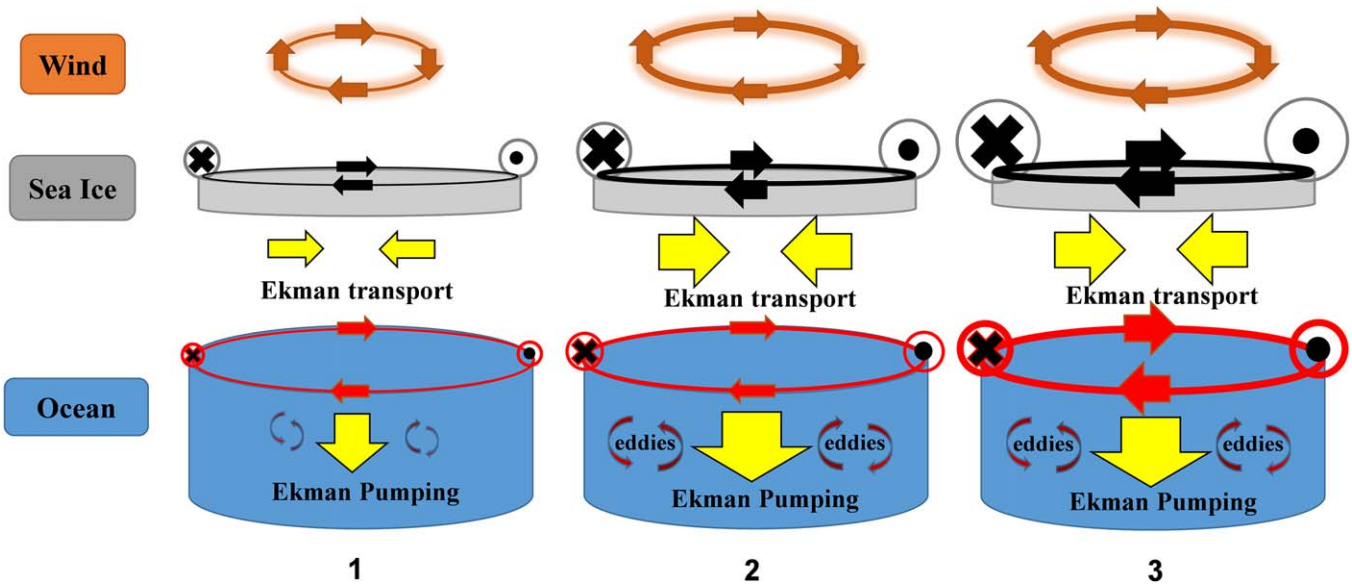


**Figure 10.** Schematic diagram of the changing Ekman dynamics in three scenarios in the Beaufort Gyre. The red arrows represent the geostrophic current. The size of the arrow represents the relative strength of each variable.

## 5. Discussion and Conclusions

This study shows that including geostrophic currents in the calculation of ice-ocean stress is important in realistically representing the spatial pattern and temporal variability of Ekman pumping in the western Arctic Ocean. Yang's method was in fact appropriate for the period before ~2000, when the difference of Ekman pumping among the methods that include or exclude geostrophic currents (order ~1 cm $s^{-1}$) was relatively small (Figures 3c, 3d and 8c, 8e). However, during 2003–2014, neglecting geostrophic currents yields an overestimate of the multiyear mean Ekman pumping velocity within the BG by up to 52%. The reason for the overestimation is that the magnitude of the ice-ocean stress curl is relatively maintained when the geostrophic current substantially increases in 2000s. The Ekman pumping is intensified during 2002–2014 (with a multiyear mean value of $-2.5$ cm $d^{-1}$) comparing with 1992–2001 (with a multiyear mean value of $-1.8$ cm $d^{-1}$) from model results. But there are no significant trend of Ekman pumping and Ekman transport during 2002–2014 (Figure 3d, supporting information Figure S2d, and Figure 8f) instead they are rather stable during this period (Figure 8f). We propose this as another mechanism to moderate the spin-up of BG and the increase of freshwater content, in addition to the eddy dissipation mechanism (e.g., Kwok & Morison, 2017; Manucharyan & Spall, 2016; Yang et al., 2016; Zhang et al., 2016; Zhao et al., 2016). In Figure 3 and Table 2, "Model 2" shows that the model vertical velocity is generally weaker than the derived Ekman pumping in "Model 1" and "Model 3" based on the surface stress especially during 2007–2014. This discrepancy may result from the eddy dissipation as it moderates the increasing vertical velocity (Figure 10). Details of eddy effects in balancing the increasing Ekman pumping from observation are discussed in Meneghello et al. (2017).

The inclusion of geostrophic currents leads to several upwelling regions, i.e., the region near the Chukchi Abyssal Plain, the northern and southern Canada Basin (Figure 2). The upwelling patches become more prevalent and stronger in the southern Canada Basin and the Chukchi Abyssal Plain as the oceanic BG spin-up (Figure 7b and supporting information Figures S1b, S1c). A recent study by Timmermans et al. (2017) shows an upwelling region at the southern limb of the BG (the negative subduction value in the southern Canada Basin in their supporting information Figures S2c, S2d), similar to our results. Our results suggest that the changing pathways of Pacific inflow water (e.g., Brugler et al., 2014; Steele et al., 2004) may be related to the changing position of the BG and the intensification of geostrophic currents in the southwestern Canada Basin. In this way, more Pacific Water is subducting in the northern Chukchi Sea and swept along geostrophic contours downward and northward into the gyre, following a helical pathway (Timmermans et al., 2014), which in turn could be an important freshwater resource that feeds the Canada Basin when the BG spins up.

Based on our results, we have identified three scenarios of differing Ekman dynamics (Figure 10). In the first scenario, the surface wind, sea ice motion, and geostrophic current were all generally weak, with weak spatial gradients and thus weak Ekman pumping (Figures 7b, supporting information Figures S1b, S1c, and Figures 8a–8c). The years 1992–2001 could fit roughly into this scenario if excluding three relatively high downwelling years in 1995, 1997, and 1998 (Figure 3d and supporting information Figure S2d). In the second scenario, the surface winds and sea ice motion accelerated (Figures 8a and 8b, also see Giles et al., 2012); geostrophic currents also began to increase (Figure 8c), although at a slower rate owing to the large inertia in the ocean system. Ekman transport and pumping thus reached high values during this time, owing to the large difference between sea ice motion and geostrophic current (i.e., ice-ocean shear) (Figures 3d and 8e). The years 2002–2008 could be fit roughly into this scenario as a transition periods. In the third scenario, surface winds remain relatively unchanged, but both the sea ice motion and geostrophic current reached their maximum (Figures 8b and 8c), possibly influenced in part by changes in sea ice dynamics (Zhang et al., 2016). As a result, the shear between sea ice and ocean movement remains unchanged relative to that in the second scenario, resulting in relatively stable Ekman transport and downwelling in the center of the BG (Figures 3d, 8f, 7b and supporting information Figures S1b, S1c). The years 2009–2014 could be roughly categorized into this scenario. In contrast to the situation in the central BG, the inflowing Pacific Water combined with the intensified sea ice motion to induce a southwestward ice-ocean stress and northwestward Ekman convergence and downwelling in the Chukchi Sea, this downwelling intensified during the periods of 2003–2008 (Figure 7b and supporting information Figures S1b, S1c). Overall, these scenarios are closely linked to the changes in surface forcing (wind/sea ice) and hydrographic adjustment (geostrophic current increasing). These two factors should be properly evaluated when considering the Ekman dynamics in the western Arctic Ocean.

A possible way to evaluate the Ekman pumping velocity from in situ observation was used in McPhee et al. (2009) and Jackson et al. (2010). In these studies, they used the deepening depth of the Near-Surface Temperature Maximum layer (NSTM) over several months to derive the Ekman pumping velocity. However, there are many uncertainties using this method. The deepening of the NSTM layer is not a process that is determined solely by Ekman pumping; wind-induced mixing could also deepen the NSTM layer. The location that McPhee et al. (2009) chose to derive Ekman pumping velocity is far north of the BG center (comparing with the multiyear mean BG center from all methods, Figure 2), so that changes in NSTM depth may be strongly influenced by other processes besides pumping (e.g., advective flux convergence, thermodynamics) that might be significant at the outer rim of the BG. We compared McPhee's Ekman pumping velocity estimate of $-11.7$ cm $d^{-1}$ at this location during the same period using our seven methods. The results from almost all of methods show a relatively weak downwelling rate with less than half of that value (supporting information Table S1). We also found it difficult to identify a consistent deepening of the NSTM over months in a stationary location inside BG (south of 76°N) using Ice-Tethered Profiler data (Krishfield et al., 2008). Thus, we could not validate the Ekman pumping velocity using this method. Further study is needed to better evaluate Ekman pumping velocity using hydrographic observations.

We also show that using modeled vertical velocity fields just below the mixed layer (the method of Model 2) provides a very good estimate of Ekman pumping (as assumed by Timmermans et al. (2017)). At the same time, we acknowledge that our model does have some bias in simulating the domain of the BG and its central position, relative to lower-resolution satellite observations. On the other hand, the Ekman pumping which is derived using the monthly DOT-derived geostrophic current may also have some uncertainties in ice-ocean shear since it may underestimate the spatial gradient of geostrophic current and thus the spatial gradient of ice-ocean stress and the final ice-ocean stress curl (or Ekman pumping).

**Acknowledgments**
We thank the editor (Andrey Proshutinsky), Gianluca Meneghello, and two anonymous reviewers whose thorough and kind comments helped to improve the manuscript. This study is supported by the National Key Basic Research Program of China (Program 973) (grant 2015CB953900), the National Natural Science Foundation of China (grant 41330960 and 41706211), the Office of Naval Research (grant N00014-12-1–0112), and the NSF Office of Polar Programs (PLR-1416920, PLR-1503298, PLR-1602985, ARC-1203425). We thank James Morison for helpful discussion and Barry Ma for providing the data using PHC methods for comparison. Wenli Zhong (201606335011) is supported by the China Scholarship Council for his visit to APL. The SLP data are available at http://www.esrl.noaa.gov/psd/data/gridded/. The sea ice velocity and concentration data are distributed by NSIDC (https://nsidc.org/data/nsidc-0116; http://nsidc.org/data/nsidc-0079). The PHC data are available from http://psc.apl.washington.edu/nonwp_projects/PHC/Climatology.html, in version 3.0. The monthly Arctic Dynamic Ocean Topography data are distributed by CPOM (http://www.cpom.ucl.ac.uk/dynamic_topography/). The IBCAO Bathymetry data are available from NASA (http://www.ngdc.noaa.gov/mgg/bathymetry/arctic/arctic.html). All data set were downloaded before February 2017. Model output used for our analyses presented in this paper are available from http://jmp.sh/v/ZtGu8GAxNQdSrvwevBhG. We appreciate the support and helpful scientific discussions associated with the Forum for Arctic Modeling and Observational Synthesis (FAMOS) and the FAMOS School for Young Arctic Scientists.

## References

Armitage, T. W., Bacon, S., Ridout, A. L., Thomas, S. F., Aksenov, Y., & Wingham, D. J. (2016). Arctic sea surface height variability and change from satellite radar altimetry and GRACE, 2003–2014. *Journal of Geophysical Research: Oceans*, *121*, 4303–4322. https://doi.org/10.1002/2015JC011579

Armitage, T. W. K., Bacon, S., Ridout, A. L., Petty, A. A., Wolbach, S., & Tsamados, M. (2017). Arctic Ocean surface geostrophic circulation 2003–2014. *The Cryosphere*, *11*, 1767–1780. https://doi.org/10.5194/tc-11-1767-2017

Brugler, E. T., Pickart, R. S., Moore, G. W. K., Roberts, S., Weingartner, T. J., & Statscewich, H. (2014). Seasonal to interannual variability of the Pacific water boundary current in the Beaufort Sea. *Progress in Oceanography*, *127*, 1–20.

Cole, S. T., Toole, J. M., Lele, R., Timmermans, M. L., Gallaher, S. G., Stanton, T. P.,. . . Haas, C. (2017). Ice and ocean velocity in the Arctic marginal ice zone: Ice roughness and momentum transfer. *Elementa: Science of the Anthropocene*, *5*, 55. http://doi.org/10.1525/elementa.241

Comiso, J. C. (2000). Updated 2015: *Bootstrap sea ice concentrations from Nimbus-7 SMMR and DMSP SSM/I-SSMIS, version 2. [Northern Hemisphere/Daily]*. Boulder, CO: NASA National Snow and Ice Data Center Distributed Active Archive Center. https://doi.org/10.5067/J6JQLS9EJ5HU

Gaube, P., Chelton, D. B., Samelson, R. M., Schlax, M. G., & O'neill, L. W. (2015). Satellite observations of mesoscale eddy induced Ekman pumping. *Journal of Physical Oceanography*, *45*, 104–132. https://doi.org/10.1175/JPO-D-14-0032.1

Giles, K. A., Laxon, S. W., Ridout, A. L., Wingham, D. J., & Bacon, S. (2012). Western Arctic Ocean freshwater storage increased by wind-driven spin-up of the Beaufort Gyre. *Nature Geoscience*, *5*, 194–197.

Hibler, W. D. III (1979). A dynamic thermodynamic sea ice model. *Journal of Physical Oceanography*, *9*(4), 815–846.

Hibler, W. D., & Bryan, K. (1987). A diagnostic ice ocean model. *Journal of Physical Oceanography*, *17*, 987–1015. https://doi.org/10.1175/1520-0485(1987)017<0987:ADIM>2.0.CO;2

Jackson, J. M., Carmack, E. C., McLaughlin, F. A., Allen, S. E., & Ingram, R. G. (2010). Identification, characterization, and change of the near-surface temperature maximum in the Canada Basin, 1993–2008. *Journal of Geophysical Research*, *115*, C05021. https://doi.org/10.1029/2009JC005265

Jakobsson, M., Mayer, L., Coakley, B., Dowdeswell, J. A., Forbes, S., Fridman, B.,. . . Weatherall, P. (2012). The International Bathymetric Chart of the Arctic Ocean (IBCAO) Version 3.0. *Geophysical Research Letters*, *39*, L12609. https://doi.org/10.1029/2012GL052219

Kalnay, E., Kanamitsu, M., Kistler, R., Collins, W., Deaven, D., Gandin, L.,. . . Joseph, D. (1996). The NCEP/NCAR 40-year reanalysis project. *Bulletin of the American Meteorological Society*, *77*, 437–471.

Krishfield, R., Toole, J., Proshutinsky, A., & Timmermans, M.-L. (2008). Automated ice-tethered profilers for seawater observations underpack ice in all seasons. *Journal of Atmospheric and Oceanic Technology*, *25*, 2091–2095. https://doi.org/10.1175/2008JTECHO587.1

Kwok, R., & Morison, J. (2017). Recent changes in Arctic sea ice and ocean circulation. *US CLIVAR Variations* (Summer 2017), *15*(3), 1–6.

Lindsay, R., Wensnahan, M., Schweiger, A., & Zhang, J. (2014). Evaluation of seven different atmospheric reanalysis products in the Arctic. *Journal of Climate*, *27*, 2588–2606. https://doi.org/10.1175/JCLI-D-13-00014.1

Ma, B., Steele, M., & Lee, C. M. (2017). Ekman circulation in the Arctic Ocean: Beyond the Beaufort Gyre. *Journal of Geophysical Research: Oceans*, *122*, 3358–3374. https://doi.org/10.1002/2016JC012624

Manucharyan, G. E., & Spall, M. A. (2016). Wind-driven freshwater buildup and release in the Beaufort Gyre constrained by mesoscale eddies. *Geophysical Research Letters*, *43*, 273–282. https://doi.org/10.1002/2015GL065957

Martin, T., Steele, M., & Zhang, J. (2014). Seasonality and long-term trend of Arctic Ocean surface stress in a model. *Journal of Geophysical Research: Oceans*, *119*, 1723–1738. https://doi.org/10.1002/2013JC009425

McLaughlin, F. A., & Carmack, E. C. (2010). Deepening of the nutricline and chlorophyll maximum in the Canada Basin interior, 2003–2009. *Geophysical Research Letters*, *37*, L24602. https://doi.org/10.1029/2010GL045459

McPhee, M. G. (1975). Ice-momentum transfer for the AIDJEX ice model. *AIDJEX Bulletin*, *29*, 93–112.

McPhee, M. G. (1980). An analysis of pack ice drift in summer. In R. Pritchard (Ed.), *Sea ice processes and models* (pp. 62–75). Seattle, WA: University of Washington Press.

McPhee, M. G. (2013). Intensification of geostrophic currents in the Canada Basin, Arctic Ocean. *Journal of Climate*, *26*(10), 3130–3138.

McPhee, M. G., Proshutinsky, A., Morison, J. H., Steele, M., & Alkire, M. B. (2009). Rapid change in freshwater content of the Arctic Ocean. *Geophysical Research Letters*, *36*, L10602. https://doi.org/10.1029/2009GL037525

Meneghello, G., Marshall, J., Cole, S. T., & Timmermans, M.-L. (2017). Observational inferencesof lateral eddy diffiusivity in the halocline of the Beaufort Gyre. *Geophysical Research Letters*, *44*. https://doi.org/10.1002/2017GL075126

Niiler, P. P. (1969). On the Ekman divergence in an oceanic jet. *Journal of Geophysical Research*, *74*, 7048–7052. https://doi.org/10.1029/JC074i028p07048

Peralta-Ferriz, C., & Woodgate, R. A. (2015). Seasonal and interannual variability of pan-Arctic surface mixed layer properties from 1979 to 2012 from hydrographic data, and the dominance of stratification for multiyear mixed layer depth shoaling. *Progress in Oceanography*, *134*, 19–53.

Pickart, R. S., Moore, G. W. K., Torres, D. J., Fratantoni, P. S., Goldsmith, R. A., & Yang, J. (2009). Upwelling on the continental slope of the Alaskan Beaufort Sea: Storms, ice, and oceanographic response. *Journal of Geophysical Research*, *114*, C00A13. https://doi.org/10.1029/2008JC005009

Pickart, R. S., Spall, M. A., Moore, G. W. K., Weingartner, T. J., Woodgate, R. A., Aagaard, K., & Shimada, K. (2011). Upwelling in the Alaskan Beaufort Sea: Atmospheric forcing and local versus non-local response. *Progress in Oceanography*, *88*, 78–100. https://doi.org/10.1016/j.pocean.2010.11.005

Proshutinsky, A., Bourke, R. H., & McLaughlin, F. A. (2002). The role of the Beaufort Gyre in Arctic climate variability: Seasonal to decadal climate scales. *Geophysical Research Letters*, *29*(23), 2100. https://doi.org/10.1029/2002GL015847

Proshutinsky, A., Dukhovskoy, D., Timmermans, M.-L., Krishfeld, R., & Bamber, J. L. (2015). Arctic circulation regimes. *Philosophical Transactions of the Royal Society A*, *373*, 20140160. https://doi.org/10.1098/rsta.2014.0160

Proshutinsky, A., Krishfield, R., Timmermans, M.-L., Toole, J., Carmack, E., McLaughlin, F.,. . . Shimada, K. (2009). Beaufort Gyre freshwater reservoir: State and variability from observations. *Journal of Geophysical Research*, *114*, C00A10. https://doi.org/10.1029/2008JC005104

Steele, M., Morison, J., Ermold, W., Rigor, I., Ortmeyer, M., & Shimada, K. (2004). Circulation of summer Pacific halocline water in the Arctic Ocean. *Journal of Geophysical Research*, *109*, C02027. https://doi.org/10.1029/2003JC002009

Steele, M., Morley, R., & Ermold, W. (2001). PHC: A global ocean hydrography with a high-quality Arctic Ocean. *Journal of Climate*, *14*, 2079–2087.

Stern, M. E. (1965). Interaction of a uniform wind stress with a geostrophic vortex. *Deep Sea Research and Oceanographic Abstracts*, *12*, 355–367. https://doi.org/10.1016/0011-7471(65)90007-0

Sumata, H., Gerdes, R., Kauker, F., & Karcher, M. (2015). Empirical error functions for monthly mean Arctic sea-ice drift. *Journal of Geophysical Research: Oceans*, *120*, 7450–7475. https://doi.org/10.1002/2015JC011151

Szanyi, S., Lukovich, J. V., Barber, D. G., & Haller, G. (2016). Persistent artifacts in the NSIDC ice motion data set and their implications for analysis. *Geophysical Research Letters*, *43*, 10,800–10,807. https://doi.org/10.1002/2016GL069799

Timmermans, M.-L., Marshall, J., Proshutinsky, A., & Scott, J. (2017). Seasonally derived components of the Canada Basin halocline. *Geophysical Research Letters*, *44*, 5008–5015. https://doi.org/10.1002/2017GL073042

Timmermans, M.-L., Proshutinsky, A., Golubeva, E., Jackson, J. M., Krishfield, R., McCall, M., & Platov, G. (2014). Mechanisms of Pacific summer water variability in the Arctic's central Canada Basin. *Journal of Geophysical Research: Oceans*, *119*, 7523–7548. https://doi.org/10.1002/2014JC010273

Tsamados, M., Feltham, D., Schroeder, D., Flocco, D., Farrell, S., Kurtz, N., Laxon, S., & Bacon, S. (2014). Impact of variable atmospheric and oceanic form drag on simulations of Arctic sea ice. *Journal of Physical Oceanography*, *44*, 1329–1353. https://doi.org/10.1175/JPO-D-13-0215.1

Tschudi, M., Fowler, C., Maslanik, J., Stewart, J. S., & Meier, W. (2016). *Polar pathfinder daily 25 km EASE-grid sea ice motion vectors, version 3. [Indicate subset used]*. Boulder, CO: NASA National Snow and Ice Data Center Distributed Active Archive Center. https://doi.org/10.5067/O57VAIT2AYYY

Watanabe, E. (2013). Linkages among halocline variability, shelf-basin interaction, and wind regimes in the Beaufort Sea demonstrated in pan-Arctic Ocean modeling framework. *Ocean Modelling*, *71*, 43–53. https://doi.org/10.1016/j.ocemod.2012.12.010

Watanabe, E., & Ogi, M. (2013). How does Arctic summer wind modulate sea ice-ocean heat balance in the Canada Basin? *Geophysical Research Letters*, *40*, 1569–1574. https://doi.org/10.1002/grl.50363

Wenegrat, J. O., & Thomas, L. N. (2017). Ekman transport in balanced currents with curvature. *Journal of Physical Oceanography*, *47*, 1189–1203. https://doi.org/10.1175/JPO-D-16-0239.1

Weingartner, T., Aagaard, K., Woodgate, R., Danielson, S., Sasaki, Y., & Cavalieri, D. (2005). Circulation on the north central Chukchi Sea shelf. *Deep Sea Research, Part II*, *52*, 3150–3174.

Yang, J. (2006). The seasonal variability of the Arctic Ocean Ekman transport and its role in the mixed layer heat and salt fluxes. *Journal of Climate*, *19*, 5366–5387. https://doi.org/10.1175/JCLI3892.1

Yang, J. (2009). Seasonal and interannual variability of downwelling in the Beaufort Sea. *Journal of Geophysical Research*, *114*, C00A14. https://doi.org/10.1029/2008JC005084

Yang, J., Proshutinsky, A., & Lin, X. (2016). Dynamics of an idealized Beaufort Gyre: 1. The effect of a small beta and lack of western boundaries. *Journal of Geophysical Research: Oceans*, *121*, 1249–1261. https://doi.org/10.1002/2015JC011296

Zhang, J., Steele, M., Runciman, K., Dewey, S., Morison, J., Lee, C., . . . Toole, J. (2016). The Beaufort gyre intensification and stabilization: A model-observation synthesis. *Journal of Geophysical Research: Oceans*, *121*, 7933–7952. https://doi.org/10.1002/2016JC012196

Zhao, M., Timmermans, M. L., Cole, S., Krishfield, R., & Toole, J. (2016). Evolution of the eddy field in the Arctic Ocean's Canada Basin, 2005–2015. *Geophysical Research Letters*, *43*(15), 8106–8114.

Zhong, W., Zhao, J., Shi, J., & Cao, Y. (2015). The Beaufort Gyre variation and its impacts on the Canada Basin in 2003–2012. *Acta Oceanologica Sinica*, *34*(7), 19–31. https://doi.org/10.1007/s13131-015-0657-0